

A linked geomorphological and geophysical modelling methodology applied to an active landslide

1 Authors

Jimmy Boyd^{1,2}, Jonathan Chambers¹, Paul Wilkinson¹, Maria Peppas³, Arnaud Watlet¹, Matt Kirkham¹, Lee Jones¹, Russel Swift¹, Phil Meldrum¹, Sebastian Uhlemann⁴, Andrew Binley²

1.1 Affiliations

- 1) The British Geological Survey, Nottingham, UK
- 2) Lancaster University, Lancaster, UK
- 3) Newcastle University, Newcastle, UK
- 4) Earth and Environmental Sciences Area – Berkley Lab, Berkley, California, USA

Corresponding email, Jimmy Boyd: jamyd91@bgs.ac.uk

1.2 Orcid IDs (where known/applicable)

Jimmy Boyd – 0000-0002-3748-8535

Jonathon Chambers - 0000-0002-8135-776X

Maria Peppas - 0000-0001-9683-0217

Arnaud Watlet - 0000-0003-0318-9032

Lee Jones - 0000-0003-4825-7238

Sebastian Uhlemann - 0000-0002-7673-7346

Andrew Binley - 0000-0002-0938-9070

2 Abstract

Moisture-induced landslides are a global geohazard; mitigating the risk posed by landslides requires an understanding of the hydrological and geological conditions present within a given slope. Recently, numerous geophysical studies have been attempted to characterise slow moving landslides, with an emphasis on developing geoelectrical methods as a hydrological monitoring tool. However, landslides pose specific challenges for processing geoelectrical data in long-term monitoring contexts as the sensor arrays can move with slope movements. Here we present an approach for processing long-term (over 8 years) geoelectrical monitoring data from an active slow moving landslide, Hollin Hill, situated in Lias rocks in the southern Howardian Hills, UK. These slope movements distorted the initial setup of the monitoring array and need to be incorporated into a time-lapse resistivity processing workflow to avoid imaging artefacts. We retrospectively sourced seven digital terrain models to inform the topography of our imaging volumes, which were acquired by either Unmanned

1 Aerial Vehicle (UAV)-based photogrammetry or terrestrial laser ranging systems. An irregular grid of
2 wooden pegs was periodically surveyed with a global position system, from which distortions to the
3 terrain model and electrode positions can be modelled with thin plate splines. In order to effectively
4 model the time-series electrical resistivity images, a baseline constraint is applied within the inversion
5 scheme; the result of the study is a time-lapse series of resistivity volumes which also incorporate
6 slope movements. The workflow presented here should be adaptable for other studies focussed on
7 geophysical/geotechnical monitoring of unstable slopes.
8
9

10 **3 Keywords**

11 Geophysics, geoelectrical monitoring, landslides, hillslope hydrogeology, landslide movements
12

13 **4 Declarations**

14 *4.1 Acknowledgements*

15 We would like to thank Josie Gibson, Frances Standen and James Standen for their continued support
16 of our monitoring activities at Hollin Hill. This work is supported by the NERC Envision Doctoral
17 Training Program (NE/L002604/1).
18

19 *4.2 Data availability*

- 20 • Geoelectrical and GPS tracking data presented here is not publically available but enquires
21 are welcome to the authors, please contact Jon Chambers of the British Geological Survey,
22 jecha@bgs.ac.uk, or the corresponding author.
23
- 24 • UAV surveying data is publically available at <https://doi.org/10.17634/154300-58>
25

26 *4.3 Code availability*

- 27 • Cloud compare – point cloud management software, open source, found at
28 <https://www.danielgm.net/cc/>
29
- 30 • ResIPy – python package for processing geoelectrical data, open source, found at
31 <https://gitlab.com/hkex/pyr2>
32
- 33 • E4D – electrical resistivity imaging code, freely available/open source, found at
34 <https://www.pnnl.gov/get-e4d>
35
- 36 • A custom set of python modules were produced during this study (not publically available at
37 time of writing).
38
- 39 • QGIS – GIS software (used for figures), open source: <https://www.qgis.org/en/site/>
40
- 41 • Inkscape – Vector based graphics editing (used for figures), open source: <https://inkscape.org/>
42
- 43 • Matplotlib – A python package for plotting and visualising data (used for figures), open
44 source: <https://matplotlib.org/>
45
46
47
48
49
50
51
52
53
54
55
56
57
58
59
60
61
62
63
64
65

- Paraview – A 3D visualisation and data analysis suite (used to produce figures), also open source: <https://www.paraview.org/>

4.4 *Conflicts of interest*

No known conflicts of interest

1
2
3
4
5
6
7
8
9
10
11
12
13
14
15
16
17
18
19
20
21
22
23
24
25
26
27
28
29
30
31
32
33
34
35
36
37
38
39
40
41
42
43
44
45
46
47
48
49
50
51
52
53
54
55
56
57
58
59
60
61
62
63
64
65

[Click here to view linked References](#)

1 Introduction

Landslides are a global phenomenon, resulting in severe economic and societal losses, and as such represent a significant geohazard. The majority of land slip events are moisture-induced (Gasmo et al. 2000), whereby increases in subsurface moisture change the pore pressure conditions which consequently affect the shear strength within a slope, resulting in slope failure (e.g., Terzaghi 1936). In order to manage this hazard, it is necessary to characterise landslide bodies both internally and externally. The external geomorphology of unstable slopes can be characterised directly with observations, aerial imagery and laser ranging methods. Determining the internal structure of landslides remains more challenging, often practitioners need to rely on point sensors and physical samples (recovered from pits or core). Over the past few decades, several studies and reviews have investigated the use of geophysical methods for landslide investigation since they are spatially sensitive, non – invasive and comparatively inexpensive relative to conventional shallow borehole investigations (Jongmans and Garambois 2007; Pazzi et al. 2019; Whiteley et al. 2019). Bogoslovsky and Ogilvy (1977) first demonstrated that geoelectrical techniques could be used to make interpretations on the structure of landslides and likely hydrological conditions, as relationships between electrical resistivity and moisture content have been long established (e.g., Archie 1947).

Numerous studies have shown electrical resistivity imaging (ERI), also known as electrical resistivity tomography (ERT), can be an invaluable aid in interpreting changes in near surface hydrologic conditions (Binley et al. 2015; Brunet et al. 2010; Chambers et al. 2014; Johnson et al. 2017; McLachlan et al. 2020; Perrone et al. 2014; Revil et al. 2020; Uhlemann et al. 2017; Uhlemann et al. 2016b). In the absence of any changes to geological structure, changes in electrical resistivity should be due to changes in temperature and the pore fluid (saturation/salinity) in the subsurface (Waxman and Smits 1968). Hence, ERI has proven to be a powerful tool when used in a hydrological monitoring context (Johnson et al. 2017; Uhlemann et al. 2017). The motivation for conducting time-lapse geoelectrical surveys on landslides is clear; the relationships between moisture content and resistivity show these methods can be used to infer the hydrological state of a hillslope and by extension shear strength and liquid limits, key parameters in estimating slope stability. For this reason the number of geoelectrical studies in landslide prone areas has been increasing in recent years (Pazzi et al. 2019; Whiteley et al. 2019). Uhlemann et al. (2017) investigated the use of the Waxman-Smits relationship (Waxman and Smits 1968) for monitoring seasonal moisture content fluctuations in an active landslide over a 3 year time period, showing that elevated moisture content derived from ERI measurements can be associated with slope movements. Crawford and Bryson (2018) presented a novel study directly relating electrical conductivity (the inverse of resistivity) to soil suction which is then used to compute an unsaturated shear strength. Recently, Revil et al. (2020) demonstrated the use of the time domain induced polarisation (IP) method for use in clay rich, landslide prone, materials, transforming their geoelectrical models into both a soil moisture content estimates and cation exchange capacities through petrophysical calibration. Once these parameters have been estimated a volumetric approximation of permeability can be attempted (Soueid Ahmed et al. 2020), hence this method may have future implications for coupled geoelectrical and hydrological modelling. The focus here is the more widely used ERI method for monitoring landslides.

38 The question addressed in this study is how to process long term data on an active landslide? It is imperative
39 that workflows are developed to process time-lapse geoelectrical datasets in a timely and robust manner, as by
40 their nature landslides can have multiple data processing challenges associated with them. Misplaced electrodes
41 (in the geophysical model) have potential fields which are incorrectly reproduced in geoelectrical imaging,
42 therefore the user of geoelectrical monitoring must have a good understanding of both the surface topography
43 and electrode placement of a given field site before attempting any geophysical method. Foremost, if the
44 landslide is active then it is likely that the surface will be altered throughout the monitoring period, and secondly
45 permanently installed electrodes are likely to have translated with surface movements. The latter has been
46 addressed in the literature as the movements of electrodes mask any changes in resistivity due to moisture
47 contents and can cause significant artefacts in the resistivity images if not accounted for in geophysical
48 processing (Uhlemann et al. 2017; Uhlemann et al. 2015; Wilkinson et al. 2016; Wilkinson et al. 2010).
49 Uhlemann et al. (2015) demonstrate three interpolation techniques for interpolating electrode movements from
50 sparse topographic information at a single point in time and Wilkinson et al. (2016) reconstruct landslide
51 movements from 4D ERI monitoring data, whereby changes in the measured transfer resistances are modelled in
52 terms of the electrode displacements. However neither of the aforementioned methods addresses changes in
53 topography, although Loke et al. (2018) reconstruct topography changes from modelling electrode
54 displacements for 2D monitoring setups. Currently it is logistically difficult, and cost inefficient, to acquire
55 digital elevation models (DEMs) at a temporal resolution needed for effective geoelectrical monitoring (every 2-
56 3 days in this study). However sparse monitoring of discrete topographic points is more accessible. For example
57 Le Breton et al. (2019) demonstrate a relatively low-cost monitoring system, where unwrapped phase changes
58 recorded between a radio transmitter and a network of receivers (placed on the moving slope) are translated into
59 one-dimensional movements. The reconstruction of electrode movements with geoelectrical data (Wilkinson et
60 al. 2016) could also be used for this purpose. Here we manually survey gridded markers on a slope with
61 repeated field visits.

62 *1.1 Motivations*

63 The aim of this study is to step towards developing a universally applicable workflow for processing long-term
64 geoelectrical monitoring data on slow moving landslides that appreciates an evolving geomorphology. For a
65 reliable geoelectrical model, the practitioner must ensure electrodes are correctly positioned within the
66 geophysical modelling volume that realises the surface geometry (as is the case for near surface geophysics) to
67 ensure accurate modelling of electrical fields inside the imaging algorithm. The duration of the monitoring data
68 available to this study spans 8.5 years, which to the authors' knowledge represents one of the longest time series
69 analysis of ERI data within the literature, allowing the issues of data quality control, finite element mesh
70 generation and processing time to be explored. To validate the approach we process geoelectrical monitoring
71 data for a well-characterised site, the Hollin Hill landslide observatory (Chambers et al. 2011; Gunn et al. 2013;
72 Merritt et al. 2013) expanding on a previous study by Uhlemann et al. (2017).

73 A notable advance in this case is the inclusion of electrode and elevation changes into the finite element mesh
74 used to model resistivities. Robust processing of geoelectrical data is necessary for reliable interpretation of the
75 ERI time series and the conversion of geophysical properties to other parameters such as moisture content
76 (Archie 1947) or soil suction (Crawford and Bryson 2018). We anticipate, elements of the movement modelling

methodology presented here could be applicable for future hydro-geophysical investigations of landslides. Henceforth this paper aims to produce *i*) an efficient solution for interpolating landslide movements from a sparse grid *ii*) time-lapse landslide surface and distortion maps of electrode arrays *iii*) time-lapse 3D ERI volumes which capture distortions to the surface of the slope, and geophysical parameters (electrical resistivity).

2 Field site: Hollin Hill

2.1 Geological setting

The Hollin Hill landslide observatory is situated on a south facing $\sim 12^\circ$ slope composed of Lower Jurassic, Lias group, sedimentary rocks (Figure 1). The succession is dominated by marine mudstones, and the stratigraphy of the field site in ascending order is the Redcar Mudstone (RMF), Staithes Sandstone (SSF), Whitby Mudstone (WMF) and Dogger (DF) Formations. The field site is located in the southern part of the Howardian Hills, North Yorkshire UK, near to the town of Malton (Figure 1). The background orthomosaic in Figure 1 was reconstructed from a fixed-wing Unmanned Aerial Vehicle (UAV) survey in May 2016 as described in Peppas et al. (2019). Here the WMF is the actively failing unit, and is observed to be landslide-prone elsewhere in the UK as the Lias group is geographically widespread (Hobbs et al. 2005). The unit is composed of interbedded siltstones and mudstones, which often host sideritic ironstone nodules towards its base; towards the top horizon of the WMF represents an erosional unconformity (Hobbs et al. 2005). Merritt et al. (2013) provides further details on the geological setting and geomorphological attributes of the site. According to Hungr et al. (2014) the landslide can be classified as a composite, slow clay rotational slide and earth-flow. Many movements have been attributed to translational movements at the SSF-WMF boundary resulting in lobes of reworked mudstone material accumulating downslope of the WMF outcrop (Figure 1).

Figure 1: Insert map of the Hollin Hill landslide observatory pictured in May 2016 by a fixed wing UAV (Peppas et al. 2019), a simplified borehole log intersecting the 2 major lithologies sensed by ERI (location marked on map), and the location of the ERI monitoring array (interpolated). Coordinates given in British National Grid.

2.2 Instrumentation and previous studies

The investigation of slope movements at Hollin Hill began in 2005; in the following years several geotechnical and geophysical campaigns have taken place in order to better characterise the hillslope (Chambers et al. 2011; Merritt et al. 2013). These efforts culminated in setting up a permanent observatory for studying landslide processes with state-of-the-art instrumentation. The first of these instruments was the Automated Time-lapse Electrical Resistivity Tomography (ALERT) instrument (Kuras et al. 2009; Ogilvy et al. 2009) which recorded data from March 2008 (when it was installed), and ran almost continuously up until December 2018. The electrodes were arranged in five parallel lines, 9.5m apart (Figure 2), with an initial inter-electrode spacing of 4.75 m. Each line has 32 electrodes (160 in total) buried at 0.1m depth to protect the array from animals and general field activities. The 3D monitoring array (Figure 1) was setup to characterise the hillslope from head to toe and capture resistivity changes in two flow lobes (Figure 2), referenced as the eastern and western flow lobe in this study. A grid of wooden marker pegs (45 in total) were installed at the ground surface at 20 m intervals located on the surface above electrode lines (Figure 1). Alongside the ALERT system, several piezometers, tilt meters, and shape acceleration arrays (SAAs) were installed (Uhlenmann et al. 2016a); a weather station which is part of UK COSMOS network (Stanley et al. 2019; Zreda et al. 2012) was installed on the stable part of the slope in 2014 (Figure 1).

2.3 Reactivations

Previous studies and surveys of marker pegs show there have been two major reactivations at Hollin Hill. In November 2012 tilt meters recorded displacements on the western flow lobe which corresponded to an unusually wet summer (Uhlemann et al. 2017), with activity ceasing in February 2013. Additionally a rotational failure was observed just to the east of the monitored area and captured electrodes on the easternmost part of the array (line 5 in Figure 2a). Uhlemann et al. (2017) found moisture contents derived from electrical resistivity to be comparatively higher than that recorded for previous years, suggesting the increased moisture content was driving movements. Over the monitored period the easternmost side of the monitoring array has periodically been reactivated, with lateral displacements up to 8.6 m measured by August 2018.

UAV surveys and passive seismic records (unpublished study) show that another rotational back scarp developed within the monitoring array in late April 2016 at the head of the slope, which spanned four of the array lines (1 to 4). From 2016 onwards the rotational back scarp has continued to grow, presently up to 2.5 m deep, spans 36 m in the Easting direction, and ~ 12 m in the northing direction (see Figures 1 and 2 for backscarp location).

Figure 2: A) Baseline inverted image of Hollin Hill, May 2016. Interpretation of the resistivity units based on 3D ground model proposed by Merritt et al. (2013). B) Surface resistivity in relation to a Hill shaded relief map from a UAV survey in May 2016. The ALERT and COSMOS enclosures have been masked.

2.4 Recording geomorphological changes

Approximately every 2 – 3 years, terrestrial LiDAR (light detection and ranging) scans and UAV photogrammetry surveys have been conducted in order to capture the changing topography of Hollin Hill. Both techniques are suited to site scale investigation and yield DEMs which can be used to estimate surfaces changes and generate modelling volumes in ERI. Terrestrial (or ground based) LIDAR is a well-established tool for monitoring rock falls and natural slope movements, be it through permanent monitoring solutions (Lingua et al. 2008) or repeated surveys (Delacourt et al. 2007; Guerin et al. 2021; Palenzuela et al. 2016; Rosser et al. 2007). Recent advances in structure from motion (SfM) photogrammetry have yielded centimetric resolutions such that they are comparable to terrestrial LiDAR scans and both are suited to the purposes of ERI. Recently Peppia et al. (2019) demonstrated repeated UAV surveys as a means to map landslide movements and geomorphological evolution. In addition, marker pegs were surveyed every 8 -12 weeks with real time kinematic (RTK)-Global Navigation Satellite Systems (GNSS). Over a 10 year period, lateral displacements of up to 8.6 m were recorded on the landslide, whilst vertical displacements up to 2.5 m were observed.

3 Methodology

Time-lapse ERI processing of the ALERT data is complicated by the dynamic surface topography present at Hollin Hill: electrodes have moved with the landslide, and their position cannot be directly measured given that they are buried. In addition, metre-scale geomorphological features have developed at the site during the monitoring period, the rotational back scarp feature spanning array lines 1 to 4 was not present for previous studies of the site (Uhlemann et al. 2017). From a geoelectrical processing prospective a robust approach to modelling the geoelectrical measurements should be adopted as discrete changes in topography could mask hydrological changes (as electrical current flow will be incorrectly modelled); in our approach the 3D surface in

the ERI modelling volume (and electrode coordinates) is updated according to the movements of GPS peg markers, the overall workflow is illustrated in Figure 3 and can be summarised in 3 parts:

1. Update known peg positions after an RTK-GNSS survey, superimpose slope movements on to a reference DEM to create a time-lapse surface.
2. Parse geoelectrical data (from the ALERT instrument) and perform quality analysis, this includes applying appropriate filters to raw data.
3. Combing the outputs of steps 1 and 2 to link the geomorphology of the landslide to the ERI models. Firstly, the time-lapse DEM to informs ERI mesh/modelling volume generation and secondly the geoelectrical data is inverted to produced volumetric image of the resistivity distribution for a given time step.

Figure 3: Summary flow chart of updating electrode coordinates and DEM for the time-lapse inversion workflow.

3.1 Digital Terrain models

The DEMs used in this study (Table 1) had already been processed, with the effects of vegetation and other artefacts removed, as part of previous research obtained with a fixed-wing UAV (Peppia et al. 2019) and unpublished studies.

All UAV-derived DEMs referenced here are described in Peppia et al. (2019). In brief, aerial images were acquired by a fixed wing Quest 300 UAV (www.ukspacefacilities.stfc.ac.uk), equipped with either a Panasonic Lumix DMC-LX5 or a Sony a6000 compact digital camera. The resulting point clouds were constructed through SfM photogrammetry (processed using PhotoScan, www.agisoft.com) which were used to generate final DEMs with a maximum ground sampling distance of 3 cm as explained in Peppia et al.(2019). The individual UAV-derived point clouds per survey were translated and orientated to a fixed coordinate system (Ordnance Survey Great Britain 36; OSBG36) with the inclusion of surveyed ground control points. Errors due to erroneous co-registration of subsequent UAV surveys were cross validated with benchmark GNSS observations. Areas of dense vegetation were filtered out from the UAV derived DEMs and the vertical error of the point cloud used here is estimated to be on average below 5 cm, which is sufficient for the purposes of ERI.

Of the three terrestrial LiDAR scans in this study, two surveys (2008 and 2009) were acquired using a Riegl LPM i800AH, situated on a tripod positioned at the base and halfway up the slope; the raw point cloud was post-processed in RiProfile (www.riegl.com) to remove artefacts associated with vegetation. The most recent LiDAR scan (2018) was acquired with a Leica Pegasus: Backpack Mobile Mapping Solution (Leica-Geosystems 2019) and involved a continuous walkover survey of the field site, and subsequently processed in Pegasus Manager.

Table 1: Topographic survey type and date of survey.

Survey Type	Date	Equipment	Method
LiDAR	Jul-08	Riegl LPM i800AH	Terrestrial LiDAR
LiDAR	Apr-09	Riegl LPM i800AH	Terrestrial LiDAR
UAV	Dec-14	Quest 300 UAV	Airborne Photogrammetry
UAV	Mar-15	Quest 300 UAV	Airborne Photogrammetry

UAV	Feb-16	Quest 300 UAV	Airborne Photogrammetry
UAV	May-16	Quest 300 UAV	Airborne Photogrammetry
LiDAR	Apr-18	Leica Pegasus: Backpack	Terrestrial LiDAR

187

188 Although satellite-based methods such as Interferometric Synthetic Aperture Radar (InSAR) can have
189 millimetric resolution and have been used successfully in mapping landslide movements (e.g., Booth et al.
190 2020), in our case satellite techniques were found to be inappropriate due to the lack of permanent scatterers
191 (Ferretti et al. 2001) and poor data availability during the relevant time periods.

192 3.2 Movement modelling

193 The marker pegs were surveyed using a Leica System 1200 RTK-GPS at a higher temporal frequency than the
194 acquisition of DEMs (shown with vertical lines in Figure 4), hence an interpolation scheme allows the surface of
195 the DEM to distort with the change in the peg position without the need for frequent DEM surveys (Equation 1).
196 Figure 4 (a) shows the frequency of peg and number of transfer resistance measurements passed to the inversion
197 scheme, any missing pegs are assumed to occupy their last known position.

198 *Figure 4: A) Number of transfer resistance measurements retained after parsing the ALERT data with cross line
199 measurements, including measurements in forward and reverse configurations. Dates of cable repairs and peg
200 surveys are also indicated. Summer and autumn months are greyed. B) Median contact resistance computed for
201 each day ALERT ERI survey was acquired as ALERT reports a contact resistance for each resistivity
202 measurement.*

203 We adopt a thin plate spline approach to map lateral and vertical movements on the hillslope from a discrete set
204 of points (surveying pegs in this case) for each time the points have their position recorded. The displacement
205 for any point within a grid square of the surveying pegs is given as

$$206 \mathbf{d}(x, y) = \mathbf{a}_{xx}x^2 + \mathbf{a}_{xy}xy + \mathbf{a}_{yy}y^2 + \mathbf{b}_x x + \mathbf{b}_y y + \mathbf{c} \quad \text{Equation 1}$$

207 Where \mathbf{d} is the displacement vector in the vertical and lateral directions at coordinate (x, y) , the other
208 parameters denoted \mathbf{a} , \mathbf{b} and \mathbf{c} are model vectors. This can be solved as a system of linear equations such that

$$209 \begin{bmatrix} x_1^2 & x_1 y_1 & y_1^2 & x_1 & y_1 & 1 \\ x_2^2 & x_2 y_2 & y_2^2 & x_2 & y_2 & 1 \\ x_3^2 & x_3 y_3 & y_3^2 & x_3 & y_3 & 1 \\ x_4^2 & x_4 y_4 & y_4^2 & x_4 & y_4 & 1 \end{bmatrix} \begin{bmatrix} \mathbf{a}_{xxx} & \mathbf{a}_{xxy} & \mathbf{a}_{xxz} \\ \mathbf{a}_{xyx} & \mathbf{a}_{xyy} & \mathbf{a}_{xyz} \\ \mathbf{a}_{yyx} & \mathbf{a}_{yyy} & \mathbf{a}_{yyz} \\ \mathbf{b}_{xx} & \mathbf{b}_{xy} & \mathbf{b}_{xz} \\ \mathbf{b}_{yx} & \mathbf{b}_{yy} & \mathbf{b}_{yz} \\ \mathbf{c}_x & \mathbf{c}_y & \mathbf{c}_z \end{bmatrix} = \begin{bmatrix} dx_1 & dy_1 & dz_1 \\ dx_2 & dy_2 & dz_2 \\ dx_3 & dy_3 & dz_3 \\ dx_4 & dy_4 & dz_4 \end{bmatrix} \quad \text{Equation 2}$$

210 Where for example dx_1 is the displacement in the x -direction at position x_1 . Note Equation 2 cannot be
211 computed directly as the problem is underdetermined, so Lagrange multipliers are needed to solve the system of
212 linear equations. Thin plate splines are well suited for modelling movement on Hollin Hill as they are valid for
213 an irregular grid (Wahba 1990), making use of four points of reference. Previously Uhlemann et al. (2017) used
214 a piecewise planar approach, which used the three nearest reference points to interpolate the electrode
215 movements. However, this method does not produce smoothly varying displacements across entire grid squares
216 (Figure 5). Here Equation 2 is solved in order to firstly estimate any electrode positions for a given peg survey,
217 and secondly estimate displacements in the DEM. Some parts of the slope are not subject to movements, as
218 observed from repeated field observations and peg surveys, this is the case for the outcrop of the Staithes

219 Sandstone Formation (Figure 2). Therefore, an additional constraint is placed on the interpolations of electrode
220 positions, such that electrodes downslope of the flow lobes are fixed (Figure 2 a).

221 *Figure 5: Comparison of displacement grids using the piecewise planar (Uhlemann et al. 2015) and Spline*
222 *approaches. Red dots indicate markers used to interpolate movements and are representative of the movements*
223 *observed at Hollin Hill.*

224 For each time the pegs were surveyed slope movements are modelled to produce a time series of electrode
225 coordinates and DEMs. When a LIDAR or UAV survey took place during the monitoring period, the reference
226 DEM is updated (Table 1). During the monitoring period, any broken or missing surveying pegs were replaced
227 in-situ, and at no time were the pegs returned to their starting positions (hence the interpolation scheme works
228 on an irregular grid). In order to maintain consistency between DEMs for time-lapse analysis, the point cloud
229 from each UAV or LIDAR scan (Table 1) is filtered with a 2D 1×1 m moving average window with 0.5 m
230 tolerance, to avoid interference from vegetation features left inside the DEMs. The point clouds are then down
231 sampled on to a regular 1 m grid for the purposes of ERI mesh generation using a bilinear interpolation scheme.
232 As 3 different field and processing techniques were used to acquire each DEM, the point clouds are then aligned
233 using CloudCompare (GPL-software 2020) against the DEM acquired in July 2008.

234 3.3 Time-lapse ERI acquisition and processing

235 3.3.1 Measurements

236 The ALERT system was set up to record multichannel dipole-dipole measurements (Binley and Slater 2020), for
237 both in-line and cross-line (equatorial) configurations. Raw measurements are in the form of transfer resistances
238 (TR): the ratio of a difference in voltage between two electrodes and the current injected in the other two
239 electrodes of a specific four electrode configuration. The dipole lengths, a , on inline measurements range
240 between 1 to 4 electrode spacings (4.75 to 19 m) with inter-dipole separations, na , where $n = 1-8$ (Uhlemann et
241 al. 2017). Dipole – dipole equatorial measurements are made on adjacent lines, where $a = 9.5$ m and $n = 0.5,$
242 1.0, 1.5, ..., 9.5, 10.0 (since the spacing between adjacent lines is twice the along-line spacing). The ALERT
243 data are stored by date and compiled into a time series of 3D ERI data, with 929 entries in total (Figure 4)
244 between the 21st of December 2009 to the 16th of September 2018. Note that although ALERT was installed in
245 March 2008, automated recording did not start until January 2009 and cross-line measurements were not added
246 to the ALERT scheduling files until December 2009. Generally, measurements were made every 2 - 3 days,
247 however there are data gaps due to power failures and equipment malfunctions associated with ALERT and its
248 supporting infrastructure.

249 ERI data quality varied widely during the monitoring period, this is largely driven by seasonal changes in
250 contact resistances; which were higher during summer months due to the decreased moisture content of the
251 ground surface (Figure 4 b), resulting in poorer galvanic contact between the electrodes and their surrounding
252 material. Consequently, more data are filtered out during the summers (Figure 4 a). Breakages in the electrode
253 cables (as a result of movements) rendered some electrodes inoperable, also contributing to diminished data
254 quality. The ERI cable on line 5 had to be repaired during the monitoring period due to breakages (Figure 2 a,
255 Figure 4 a), which rendered four electrodes on this line inoperable from February 2015 until October 2016. The
256 measurements are filtered out based on five criteria (two of which refer to a measurement of reciprocity (Tso et
257 al. 2017)):

1. A contact resistance over 5000 Ω , as these measurements are likely to have a high signal to noise ratio given that the environment is relatively conductive (apparent resistivities below 200 Ωm are observed).
2. An approximated apparent resistivity outside the range of 0 and 200 Ωm . Apparent resistivity is computed by multiplying the TR measurement by a geometric factor (Binley and Slater 2020), which differs depending on the array configuration, it's value is valid for homogenous flat ground. In this case positive geometric factors are anticipated due to the geometry of active electrodes, and measurements with over 200 Ωm corresponded with erroneous TR measurements which resulted in artefacts in the ERI inversions.
3. An amplitude ratio (measure of waveform symmetry) outside the range of 0.85 and 1.15. Beyond this desired range shows that the alternating current signal is asymmetrical.
4. A reciprocal error over 10%, which often taken as a standard cut off for reliable transfer resistance measurements (e.g., Carrigan et al. 2013).
5. Measurements without reciprocals, as their reliability cannot be assessed.

Generally, over 3000 individual measurements are retained for inversion (approximately 68% of viable measurements made in the forward direction).

3.3.2 Inversion workflow

As noted by Uhlemann et al. (2017) (and references therein), incorrect electrode positions within the ERI inversion lead to artefacts in the resulting model. As the ERI surveys have a higher temporal frequency than the peg surveys, a linear interpolation (using time and displacement as input) is used to sample the estimated displacements onto the days which ERI surveys took place (every ~ 3 days). This is deemed appropriate as the landslide is slow moving and significant movements are captured by the GPS surveys of the marker pegs.

For each time step in the time-lapse ERI a new mesh with unique topography and electrode nodes is generated; this is necessary to realise vertical and lateral landslide movements in the ERI inversions. The options for time-lapse inversion are therefore limited in this case. Difference inversions (LaBrecque and Yang 2001) do not allow for changing meshes or electrode positions, and time-lapse inversions with moving electrodes have only recently been demonstrated for 2D problems (Loke et al. 2014; Loke et al. 2018). Here we adopt a similar custom workflow to that of previous studies (Uhlemann et al. 2017; Whiteley et al. 2020) through a baseline-constrained approach. A nearest neighbour look up is used to translate the baseline model values onto each time-lapse mesh. Compared to Uhlemann et al. (2017), who considered a shorter time series, the inclusion of topography is necessary due to the surface changes during the timescales of this study, and whereas a fine mesh was used such that electrodes could move on the same mesh for each ERI inversion, here a coarser mesh is used during the inversion to give a comparatively modest computation time. Of the 929 datasets collected in total, 914 were processed (the rejected surveys have fewer than 500 valid measurements). The inversions were run on a high-performance cluster, across two Intel nodes each with 16 logical processing cores, taking approximately 3 days to run. The baseline inversion is taken from 15th of April 2010 as this represents a time of intermediate saturation on the hillslope, good data quality and when the landslide was not influenced by movements (Uhlemann et al. 2017).

295 We use E4D (Johnson et al. 2010) for the 3D ERI on a tetrahedral mesh, as the code scales with computational
 296 resources. Additionally the ResIPy python code is used to prepare data for inversion (Blanchy et al. 2019).
 297 Weighting the measured transfer resistances by a reciprocal error model has been shown to produce more robust
 298 results (Tso et al. 2017), therefore for each ERI step a unique reciprocal error model is computed based on
 299 multi-bin analysis (Binley and Slater 2020; Mwakanyamale et al. 2012). The average resistance of both the
 300 forward and reciprocal measurement is taken into the inversion, and the absolute reciprocal error is defined as

$$R_{error} = |R_{for} - R_{rev}| \quad \text{Equation 3}$$

301 where R_{for} and R_{rev} are transfer resistance measured in forward and reverse mode, respectively. A different
 302 error model is required for each ERI time step because of the different error characteristics present for different
 303 seasons and data quality present in the time-lapse data. For all inversions a constant 2.5% is added to the
 304 reciprocal errors to represent the forward modelling errors, as this was found to result in a spatially and
 305 temporarily smooth model comparable to previous investigations (e.g., Merritt et al. 2013). Resistivity is
 306 expected to vary smoothly from the baseline (Uhlenmann et al. 2017), and hence an L2 norm (Loke et al. 2014) is
 307 applied as a temporal constraint as well as a smoothness constraint. For time-lapse inversions a relative weight
 308 of 0.1 is used as a baseline constraint verses 0.9 for spatial constraint; this encourages a smooth spatial result
 309 over smoothed temporal changes. E4D was assigned a target Chi-squared (χ^2) value of 1.1. These parameters
 310 were found to minimise inversion artefacts, whilst converging on reasonable solutions.

311 We use a custom mesh generation scheme, a flat tetrahedral mesh is generated within Gmsh (Geuzaine and
 312 Remacle 2009), and the topography is transposed onto the mesh using triangulation interpolation. Mesh node
 313 boundary conditions are then computed, such that the upper surface of the mesh is considered a zero flux
 314 boundary (i.e., cannot transmit electrical current) and the mesh is exported into the tetgen format (Si 2015) used
 315 by E4D. The baseline inversion is done on a finer inversion mesh to encourage accurate as possible starting
 316 resistivities for each subsequent time step during nearest neighbour lookup.

3.3.3 Temperature correction

317 Electrical resistivity varies as a function of temperature, consequently time-lapse ERI volumes should be
 318 corrected for changes in seasonal temperature to avoid misinterpretation of inversion results that could
 319 otherwise be confused for hydrological changes (Chambers et al. 2014). The same seasonal depth, z , and
 320 temperature model is used to correct the inverted resistivities (post processing) here as in previous studies
 321 (Uhlenmann et al. 2017)

$$T_{model}(z, t) = T_{mean} + \frac{\Delta T}{2} \exp\left(-\frac{z}{d}\right) \sin\left(\frac{2t\pi}{365} + \varphi - \frac{z}{d}\right) \quad \text{Equation 4}$$

322 with T_{mean} as the average annual air temperature, ΔT as the difference between the largest and smallest annual
 323 temperatures, φ is a phase offset to bring surface and air temperature into phase, d is a characteristic depth and
 324 is defined as the depth where ΔT has decreased by $1/e$ (Brunet et al. 2010). t is the day in the year. The depth of
 325 the (barometric) centre of each cell in the mesh is computed, and the corrected resistivity calculated using the
 326 ratio model (Ma et al. 2011; Uhlemann et al. 2017)

$$\rho_{cor} = \rho[1 + \alpha(T_{ref} - T_{model})] \quad \text{Equation 5}$$

expressed here in terms of resistivity where ρ is the cell resistivity at temperature T_{model} , α is the temperature correction factor, set at $-0.02^{\circ}\text{C}^{-1}$, and T_{ref} is a constant reference temperature, in this case 20°C . The constants used in Equations 4 and 5 are documented by Uhlemann et al. (2017) ($T_{\text{mean}} = 10.03^{\circ}\text{C}$, $\Delta T = 15.54^{\circ}\text{C}$, $d = 2.26$ m, and $\varphi = 1.91$).

4 Results

4.1 Landslide kinematics

The modelling of the electrode movements allows for an assessment of landslide kinematics at Hollin Hill (e.g., Hutchinson 1983) over a 10 year period, Figure 6 illustrates the direction and relative magnitude of lateral electrode movements. At the end of 2012 down slope movements have been observed on the eastern flow lobe, which are accompanied up slope with a rotational failure just to the east of the monitoring array, affecting the electrodes on line 5. These movements correspond to the reactivation of the eastern flow lobe documented by Uhlemann et al. (2017) (Figure 6 b, c and S1).

We compute differences from the baseline elevation measured in 2008 (Figure 6a). The back scarp feature (spanning lines 1 to 4) is clear in the elevation models after April 2016: a decrease in the surface elevation is observed, whilst downslope of the scarp an increase in surface elevation occurs. This supports an interpretation that a rotational slip plane is present at depth; at the head of the failure a slump can be observed corresponding to an accumulation of material. After the development of the rotational back scarp feature (Figure 6) downslope displacement of the electrodes can be observed, as electrodes move with the rotating mass. Variations in elevation associated with the eastern flow lobe show a decrease near the crest of the lobe, and an increase at the head of the lobe, indicating a downslope translation of material that accumulates at the head of the flow lobe (Figure 6d). Field observations support this hypothesis, as freshly disturbed material can be observed at the toe of the flow lobe. Although movements in the mid-section of the sliding material are slight, it is also likely that this material feeds the flow lobes which move in turn. Any movements downslope on the lobes reduce the support for the upper part of the slope and further encourage the development of rotational back scarps. The observations of electrode and slope movements (as well as field visits) shows that failure at the top of the slope is progressing westward in the field area. Although beyond the scope of this study, the electrode displacements effectively provide a 3D displacement field which can be quantitatively accessed to map the slip surface at depth (Aryal et al. 2015; Booth et al. 2020).

Figure 6: Overview of elevation and electrode coordinate changes at Hollin Hill. A) Baseline hillshade, as captured by terrestrial LiDAR IN 2008, initial electrode locations (black dots), fixed electrodes (black crosses), and peg locations (blue triangles). B, C, D, E and F show the modelled displacement vectors for the electrodes and difference in elevation for November 2012, January 2013, March 2015, May 2016 and April 2018 respectively. Note part of the difference maps have been masked as the changes in these regions relate to tree cover.

Through the workflow described above (Section 3 and Figure 3), an ERI time series is produced where features such as the back scarp and flow lobes evolve naturally in the ERI inversion mesh. Figure 7 shows the development of a rotational backscarp at the head of the landslide being reproduced in the time-lapse modelling mesh which captures the inverted resistivities. The depth of the backscarp feature grows from April 2016 to December 2016.

370 *Figure 7: Time-lapse ERI results for 2016, when the back scarp was first observed.*

371 4.2 Inverse Model Validation

372 The statistical validity of inverse models are generally accessed through a value of χ^2 (Constable et al. 1987;
 373 Günther et al. 2006), in the ideal case that there are no modelling errors and data errors are fully realised a χ^2 of
 374 1 should be obtained (Johnson 2014). In this case E4D converged on a target χ^2 of 1.1 for each time-step
 375 showing reasonable fit between ERI models and the ALERT data. Note that setting a target χ^2 of 1 meant E4D
 376 could not achieve convergence for all timesteps, it can be expressed as the model misfit over the number of
 377 measurements, N , as:

$$378 \chi^2 = \frac{1}{N} [\mathbf{d} - f(\mathbf{m})]^T \mathbf{W}_d^T \mathbf{W}_d [\mathbf{d} - f(\mathbf{m})] \quad \text{Equation 6}$$

379 where \mathbf{W}_d is the data weight vector (obtained from the reciprocal error model), \mathbf{d} is the measurement vector and
 380 $f(\mathbf{m})$ is the forward response to the model parameters \mathbf{m} (Binley and Slater 2020). To assess the reliability of
 381 results we ran a separate baseline constrained inversion for March 2017 where: both electrode coordinates and
 382 topography are updated, only the electrode coordinates are updated, and neither the topography and electrode
 383 positions are updated (Figure 8), respectively these are referred to as the updated, partially updated and none
 384 updated inversions. The percentage RMS (root mean squared) error for these respective inversions are
 385 calculated as 6.9%, 7.2% and 8.2%, and hence the updated inversion (using the proposed workflow) yielded the
 386 best fit in this case. RMS in this case is defined as:

$$387 \text{RMS}(\%) = \sqrt{\frac{\sum_{i=1}^N \left[100 \frac{R_{obs_i} - R_{sim_i}}{R_{obs_i}} \right]^2}{N}} \quad \text{Equation 7}$$

388 where R_{obs} and R_{sim} are the observed and modelled transfer resistances, respectively, and N is the number of
 389 measurements. For the partially updated and none updated inversions there is a negative resistivity anomaly
 390 present on the eastern flow lobe, which is not consistent with expected resistivity changes or updated inversion.
 391 Furthermore, the updated inversion shows positive changes in resistivity compared to the baseline inversion
 392 implying relative drying, however the partially updated inversion shows an overall negative change in resistivity
 393 implying relative wetting, altering the hydrological interpretation of hill slope processes. This demonstrates the
 394 importance of topographic variations when interpreting subtle changes in resistivity as hydrological changes
 395 maybe masked if topography is not updated in the time-lapse inversion volumes.

396 *Figure 8: Comparison of a time-lapse inversion for March 2017 for A) the updated inversion, B) the partially*
 397 *updated inversion and C) the non-updated inversion.*

398 In October 2020, the ALERT system was fully decommissioned and the buried electrode arrays were recovered
 399 in preparation for the installation of a new monitoring system. It is challenging to assess the success of the
 400 interpolation scheme given the electrodes had been placed in the ground 12 years prior, as landslide movements,
 401 particularly in the flow lobes, made it difficult to relocate electrodes which had become disconnected from the
 402 buried cable. Additionally, many of the original pegs had perished and hence the quality of the interpolation
 403 likely suffered. Where the electrodes were found in place an RTK GPS was used to survey their final position,
 404 of the original 160 electrodes 108 (67.5%) were recovered. On average electrodes predicted by the interpolation
 405 were 0.51 m away from their final recorded position, the median value is 0.25 m and the standard RMS between

406 the predicted and observed displacements is 0.79 m. For context, the electrodes moved 1.79 m on average and
407 the maximum observed displacement was 7.88 m, suggesting a reasonable fit between the interpolated and
408 observed electrode positions.

409 **5 Discussion**

410 Time-lapse ERI data is difficult to visualise for multiple time steps in a static format, therefore results of the ERI
411 workflow are presented in S2. To summarise overall increases in resistivity can be observed during the summer
412 months, which is associated with decreased moisture content. Elevated moisture contents during winter months
413 are associated with lower resistivities. This is in accordance with seasonal moisture content variations observed
414 by Uhlemann et al. (2017). One approach to assess spatial and temporal variability in the resistivity results is to
415 calculate a coefficient of variation (standard deviation of each point in its time series over its mean). Although
416 each mesh in the time series is different, a nearest neighbour lookup scheme can be used to map cell resistivity
417 values onto a representative mesh, from which statistical analysis can be made as in Figure 9. The Whitby
418 mudstone downslope of the back scarp (in a rotational slump) experiences relatively little change compared to
419 the flow lobes or back scarp area whilst maintaining a relatively low resistivity, indicating the slump retains a
420 high level of moisture throughout an annual cycle. This supports previous interpretations of the hillslope
421 hydrogeology for the Hollin Hill landslide that included perched aquifers (Gunn et al. 2013; Uhlemann et al.
422 2017). It is likely positive pore pressure under the slump encourages movement on a slip plane at depth.
423 Significant changes in resistivity on the flow lobes (Figure 9) can be attributed to relative drying during the
424 summer suggesting drainage of the lobes into the SSF; and partly explained by extensional features (cracks)
425 which dominate the surface of that part of the landslide (increasing the effective porosity of the material) (Pepp
426 et al. 2019).

427 *Figure 9: Coefficient of variation volume for Hollin Hill on a representative mesh.*

428 *5.1 Workflow*

429 Through monitoring geomorphological changes, it is possible to interpret slope failure mechanisms (Hutchinson
430 1983) in this case a rotational failure is observed in slope movements. Consequently, the inclusion of time-lapse
431 DEMs likely improves the quality of inverted images (Figure 8) as the modelling of the potential field during
432 the imaging process is sensitive to surface topography, for example the development of the backscarp (over lines
433 1 – 4) would be particularly troublesome for conventional time-lapse ERI. The approach adopted here facilitates
434 a two phased interpretation through *i*) visualisation of slope movements characterising the external nature of the
435 landslide through time and *ii*) capturing the internal structure of the landslide through volumetric electrical
436 imaging which by extension can be related to moisture contents.

437 With the exception of certain models in the ERI series, which are associated with poor raw data quality
438 (particularly in 2018 when the number of TR measurements drops off significantly), the time-series analysis
439 could be taken further with petrophysical relationships between resistivity, moisture content (Uhlemann et al.
440 2017) and other critical parameters for assessing slope stability such as soil suction (Crawford and Bryson
441 2018). Alternatively, more involved workflows could conceivably couple hydrological and geoelectrical
442 modelling through petrophysical relationships (Johnson et al. 2017; Revil et al. 2020), allowing for robust
443 assessments on the slope hydrogeology through time.

444 A limitation of the workflow proposed here that it fails to account for sudden changes to the slope surface which
1 445 have been recorded by SAAs and tilt meters, rather treating alterations to the slope surface as smoothly varying
2
3 446 between different DEM surveys. We suggest further coupling between in field sensors, like SAAs, and
4
5 447 interpolation of movements to force distortions to slope topography and electrode positions to occur within
6
7 448 discrete time windows where movement is recorded. Another drawback is that the approach adopted here relies
8
9 449 on repeated field visits that are labour intensive and time consuming, hence an automated approach to
10
11 450 monitoring slope movements (Le Breton et al. 2019; Wilkinson et al. 2016) would be beneficial to future
12
13 451 studies.

13 452 **6 Conclusions**

14 453 Landslide monitoring through ERI is likely to become more pervasive in coming decades, as the method is
15
16 454 suitable for long term applications and provides volumetric estimations of hydrological parameters that
17
18 455 complements more conventional point sensors. However accurate modelling of the electrical potential field
19
20 456 requires a good understanding of the slope geomorphology, which as demonstrated here is subject to slope
21
22 457 movements if the landslide is active. Previous papers (Uhlemann et al. 2015; Wilkinson et al. 2016) have
23
24 458 addressed modelling electrode movements in ERI inversion, while this study proposes a methodology that fully
25
26 459 incorporate landslide kinematics (S1) into the inversion workflow.

26 460 Time series ERI volumes (S2) capture the changes in slope topography, necessary for avoiding imaging
27
28 461 artefacts, and electrical resistivity. Variations in the latter can be reasonably explained by seasonal fluctuations
29
30 462 in moisture content observed at Hollin Hill (Uhlemann et al. 2017). Although the 4D ERI data were processed
31
32 463 with baseline constrained inversion scheme, reasonable time-lapse results were achieved for the majority of
33
34 464 time-steps. Higher χ^2 values associated with inversions where the electrode coordinates or topography are not
35
36 465 updated demonstrate that the inversion workflow described here (Figure 3) improves the quality of inverted
37
38 466 results and is necessary for reliable hydrological interpretation of time-lapse ERI volumes. Hence establishing a
39
40 467 framework (and corresponding algorithms) for processing (hydro) geophysical datasets resulting from long term
41
42 468 monitoring solutions on active landslides.

40 469 Relationships between electrical resistivity and soil moisture are well documented, hence geoelectrical model
41
42 470 time series can be interpreted in terms of hydro-mechanical parameters through petrophysical calibrations.
43
44 471 Furthermore, linking between relevant weather data, petrophysical relationships, ERI data and landslide
45
46 472 kinematics (through the framework proposed here) could be used as forcing datasets inside of a coupled
47
48 473 hydrological modelling and ERI approach. This is a crucial step forward for developing geoelectrical landslide
49
50 474 monitoring techniques and anticipating potential failure events.

51 475 **7 References**

52 476 Archie GE (1947) Electrical resistivity an aid in core-analysis interpretation AAPG Bulletin 31:350-366
53
54
55 477 Aryal A, Brooks BA, Reid ME (2015) Landslide subsurface slip geometry inferred from 3-D surface
56
57 478 displacement fields Geophysical Research Letters 42:1411-1417 doi:<https://doi.org/10.1002/2014GL062688>
58
59
60
61
62
63
64
65

- 1 479 Binley A, Hubbard SS, Huisman JA, Revil A, Robinson DA, Singha K, Slater LD (2015) The emergence of
2 480 hydrogeophysics for improved understanding of subsurface processes over multiple scales *Water Resources*
3 481 *Research* 51:3837-3866 doi:10.1002/2015wr017016
4
5 482 Binley A, Slater L (2020) *Resistivity and Induced Polarization: Theory and Applications to the Near-Surface*
6 483 *Earth*. Cambridge University Press, Cambridge. doi:10.1017/9781108685955
7
8
9 484 Blanchy G, Saneiyani S, Boyd J, McLachlan P, Binley A (2019) ResIPy, an intuitive open source software for
10 485 complex geoelectrical inversion/modeling in 2D space.
11
12 486 Bogoslovsky VA, Ogilvy AA (1977) *Geophysical Methods for the Investigation of Landslides* *GEOPHYSICS*
13 487 42:562-571 doi:10.1190/1.1440727
14
15
16 488 Booth AM, McCarley JC, Nelson J (2020) Multi-year, three-dimensional landslide surface deformation from
17 489 repeat lidar and response to precipitation: Mill Gulch earthflow, California *Landslides* 17:1283-1296
18 490 doi:10.1007/s10346-020-01364-z
19
20
21 491 Brunet P, Clément R, Bouvier C (2010) Monitoring soil water content and deficit using Electrical Resistivity
22 492 Tomography (ERT) – A case study in the Cevennes area, France *Journal of Hydrology* 380:146-153
23 493 doi:<https://doi.org/10.1016/j.jhydrol.2009.10.032>
24
25
26 494 Carrigan CR et al. (2013) Electrical resistance tomographic monitoring of CO2 movement in deep geologic
27 495 reservoirs *International Journal of Greenhouse Gas Control* 18:401-408
28
29
30 496 Chambers J et al. (2014) 4D electrical resistivity tomography monitoring of soil moisture dynamics in an
31 497 operational railway embankment *Near Surface Geophysics* 12:61-72
32
33
34 498 Chambers JE et al. (2011) Three-dimensional geophysical anatomy of an active landslide in Lias Group
35 499 mudrocks, Cleveland Basin, UK *Geomorphology* 125:472-484
36 500 doi:<https://doi.org/10.1016/j.geomorph.2010.09.017>
37
38
39 501 Constable SC, Parker RL, Constable CG (1987) Occam's inversion: A practical algorithm for generating smooth
40 502 models from electromagnetic sounding data *GEOPHYSICS* 52:289-300 doi:10.1190/1.1442303
41
42
43 503 Crawford MM, Bryson LS (2018) Assessment of active landslides using field electrical measurements
44 504 *Engineering Geology* 233:146-159
45
46
47 505 Delacourt C et al. (2007) Remote-sensing techniques for analysing landslide kinematics: a review *Bulletin de la*
48 506 *Société Géologique de France* 178:89-100 doi:10.2113/gssgfbull.178.2.89
49
50
51 507 Ferretti A, Prati C, Rocca F (2001) Permanent scatterers in SAR interferometry *IEEE Transactions on*
52 508 *geoscience and remote sensing* 39:8-20
53
54
55 509 Gasmo JM, Rahardjo H, Leong EC (2000) Infiltration effects on stability of a residual soil slope *Computers and*
56 510 *Geotechnics* 26:145-165 doi:[https://doi.org/10.1016/S0266-352X\(99\)00035-X](https://doi.org/10.1016/S0266-352X(99)00035-X)
57
58
59 511 Geuzaine C, Remacle JF (2009) Gmsh: A 3- D finite element mesh generator with built- in pre- and post-
60 512 processing facilities *International journal for numerical methods in engineering* 79:1309-1331
61
62
63
64
65

513 GPL-software (2020) CloudCompare 2.10.2 edn.,
1
2 514 Guerin A, Jaboyedoff M, Collins BD, Stock GM, Derron M-H, Abellán A, Matasci B (2021) Remote thermal
3 515 detection of exfoliation sheet deformation Landslides 18:865-879 doi:10.1007/s10346-020-01524-1
4
5 516 Gunn D, Chambers J, Hobbs P, Ford J, Wilkinson P, Jenkins G, Merritt A (2013) Rapid observations to guide
6 517 the design of systems for long-term monitoring of a complex landslide in the Upper Lias clays of North
7 518 Yorkshire, UK Quarterly Journal of Engineering Geology and Hydrogeology 46:323-336
8
9 519 Günther T, Rücker C, Spitzer K (2006) Three-dimensional modelling and inversion of dc resistivity data
10 520 incorporating topography — II. Inversion Geophysical Journal International 166:506-517 doi:10.1111/j.1365-
11 521 246X.2006.03011.x
12
13 522 Hobbs P et al. (2005) The Engineering Geology of UK Rocks and Soils: The Lias Group British Geological
14 523 Survey IR/05/008, Nottingham, UK
15
16 524 Hungr O, Leroueil S, Picarelli L (2014) The Varnes classification of landslide types, an update Landslides
17 525 11:167-194 doi:10.1007/s10346-013-0436-y
18
19 526 Hutchinson JN (1983) Methods of locating slip surfaces in landslides Bulletin of the Association of Engineering
20 527 Geologists 20:235-252
21
22 528 Johnson T (2014) E4D: A distributed memory parallel electrical geophysical modeling and inversion code. U.S.
23 529 Department of Energy,
24
25 530 Johnson TC, Hammond GE, Chen X (2017) PFLOTRAN-E4D: A parallel open source PFLOTRAN module for
26 531 simulating time-lapse electrical resistivity data Computers & Geosciences 99:72-80
27 532 doi:<https://doi.org/10.1016/j.cageo.2016.09.006>
28
29 533 Johnson TC, Versteeg RJ, Ward A, Day-Lewis FD, Revil A (2010) Improved hydrogeophysical characterization
30 534 and monitoring through parallel modeling and inversion of time-domain resistivity and induced-polarization data
31 535 GEOPHYSICS 75:WA27-WA41 doi:10.1190/1.3475513
32
33 536 Jongmans D, Garambois S (2007) Geophysical investigation of landslides: a review Bulletin de la Société
34 537 géologique de France 178:101-112
35
36 538 Kuras O, Pritchard JD, Meldrum PI, Chambers JE, Wilkinson PB, Ogilvy RD, Wealthall GP (2009) Monitoring
37 539 hydraulic processes with automated time-lapse electrical resistivity tomography (ALERT) Comptes Rendus
38 540 Geoscience 341:868-885 doi:<https://doi.org/10.1016/j.crte.2009.07.010>
39
40 541 LaBrecque DJ, Yang X (2001) Difference inversion of ERT data: A fast inversion method for 3-D in situ
41 542 monitoring Journal of Environmental & Engineering Geophysics 6:83-89
42
43 543 Le Breton M et al. (2019) Passive radio-frequency identification ranging, a dense and weather-robust technique
44 544 for landslide displacement monitoring Engineering geology 250:1-10
45
46 545 Lieca-Geosystems (2019) Leica Pegasus:Backpack Wearable Mobile Mapping Solution.
47
48
49
50
51
52
53
54
55
56
57
58
59
60
61
62
63
64
65

- 546 Lingua A, Piatti D, Rinaudo F (2008) Remote monitoring of a landslide using an integration of GB-INSAR and
1 547 LIDAR techniques The international archives of the photogrammetry, remote sensing and spatial information
2 548 sciences 37:133-139
3
4
5 549 Loke M, Dahlin T, Rucker D (2014) Smoothness- constrained time- lapse inversion of data from 3D resistivity
6 550 surveys Near Surface Geophysics 12:5-24
7
8
9 551 Loke MH, Wilkinson PB, Chambers JE, Meldrum PI (2018) Rapid inversion of data from 2D resistivity surveys
10 552 with electrode displacements Geophysical Prospecting 66:579-594 doi:<https://doi.org/10.1111/1365-2478.12522>
11
12 553 Ma R, McBratney A, Whelan B, Minasny B, Short M (2011) Comparing temperature correction models for soil
13 554 electrical conductivity measurement Precision Agriculture 12:55-66 doi:10.1007/s11119-009-9156-7
14
15
16 555 McLachlan P, Chambers J, Uhlemann S, Sorensen J, Binley A (2020) Electrical resistivity monitoring of river-
17 556 groundwater interactions in a Chalk river and neighbouring riparian zone Near Surface Geophysics 18:385-398
18 557 doi:10.1002/nsg.12114
19
20
21 558 Merritt AJ et al. (2013) 3D ground model development for an active landslide in Lias mudrocks using
22 559 geophysical, remote sensing and geotechnical methods Landslides 11:537-550 doi:10.1007/s10346-013-0409-1
23
24
25 560 Mwakanyamale K, Slater L, Binley A, Ntarlagiannis D (2012) Lithologic imaging using complex conductivity:
26 561 Lessons learned from the Hanford 300 Area Geophysics 77:E397-E409
27
28
29 562 Ogilvy R et al. (2009) Automated monitoring of coastal aquifers with electrical resistivity tomography Near
30 563 Surface Geophysics 7:367-376
31
32
33 564 Palenzuela JA, Jiménez-Perálvarez JD, El Hamdouni R, Alameda-Hernández P, Chacón J, Irigaray C (2016)
34 565 Integration of LiDAR data for the assessment of activity in diachronic landslides: a case study in the Betic
35 566 Cordillera (Spain) Landslides 13:629-642 doi:10.1007/s10346-015-0598-x
36
37
38 567 Pazzi V, Morelli S, Fanti R (2019) A Review of the Advantages and Limitations of Geophysical Investigations
39 568 in Landslide Studies International Journal of Geophysics 2019:2983087 doi:10.1155/2019/2983087
40
41
42 569 Peppas MV, Mills JP, Moore P, Miller PE, Chambers JE (2019) Automated co- registration and calibration in
43 570 SfM photogrammetry for landslide change detection Earth Surface Processes and Landforms 44:287-303
44
45
46 571 Perrone A, Lapenna V, Piscitelli S (2014) Electrical resistivity tomography technique for landslide
47 572 investigation: a review Earth-Science Reviews 135:65-82
48
49
50 573 Revil A, Soueid Ahmed A, Coperey A, Ravel L, Sharma R, Panwar N (2020) Induced polarization as a tool to
51 574 characterize shallow landslides Journal of Hydrology 589:125369
52 575 doi:<https://doi.org/10.1016/j.jhydrol.2020.125369>
53
54
55 576 Rosser N, Lim M, Petley D, Dunning S, Allison R (2007) Patterns of precursory rockfall prior to slope failure
56 577 Journal of Geophysical Research: Earth Surface 112 doi:<https://doi.org/10.1029/2006JF000642>
57
58
59 578 Si H (2015) TetGen, a Delaunay-Based Quality Tetrahedral Mesh Generator ACM Trans Math Softw 41:Article
60 579 11 doi:10.1145/2629697
61
62
63
64
65

580 Soueid Ahmed A, Revil A, Abdulsamad F, Steck B, Vergnault C, Guihard V (2020) Induced polarization as a
581 tool to non-intrusively characterize embankment hydraulic properties Engineering Geology 271:105604
582 doi:<https://doi.org/10.1016/j.enggeo.2020.105604>

583 Stanley S et al. (2019) Daily and sub-daily hydrometeorological and soil data (2013-2017) [COSMOS-UK].
584 NERC Environmental Information Data Centre,

585 Terzaghi Kv The shearing resistance of saturated soils and the angle between the planes of shear. In:
586 Proceedings of the 1st international conference on soil mechanics and foundation engineering, 1936. Harvard
587 University Press Cambridge, MA, pp 54-56

588 Tso C-HM et al. (2017) Improved characterisation and modelling of measurement errors in electrical resistivity
589 tomography (ERT) surveys Journal of Applied Geophysics 146:103-119

590 Uhlemann S et al. (2017) Four-dimensional imaging of moisture dynamics during landslide reactivation Journal
591 of Geophysical Research: Earth Surface 122:398-418 doi:10.1002/2016JF003983

592 Uhlemann S et al. (2016a) Assessment of ground-based monitoring techniques applied to landslide
593 investigations Geomorphology 253:438-451 doi:<https://doi.org/10.1016/j.geomorph.2015.10.027>

594 Uhlemann S, Wilkinson PB, Chambers JE, Maurer H, Merritt AJ, Gunn DA, Meldrum PI (2015) Interpolation
595 of landslide movements to improve the accuracy of 4D geoelectrical monitoring Journal of Applied Geophysics
596 121:93-105 doi:<https://doi.org/10.1016/j.jappgeo.2015.07.003>

597 Uhlemann SS et al. (2016b) Integrated time-lapse geoelectrical imaging of wetland hydrological processes
598 Water Resources Research 52:1607-1625 doi:10.1002/2015WR017932

599 Wahba G (1990) Spline Models for Observational Data. Spline Models for Observational Data.
600 doi:10.1137/1.9781611970128

601 Waxman MH, Smits L (1968) Electrical conductivities in oil-bearing shaly sands Society of Petroleum
602 Engineers Journal 8:107-122

603 Whiteley J, Chambers J, Uhlemann S, Wilkinson P, Kendall J (2019) Geophysical monitoring of moisture-
604 induced landslides: a review Reviews of Geophysics 57:106-145

605 Whiteley JS et al. (2020) Landslide monitoring using seismic refraction tomography – The importance of
606 incorporating topographic variations Engineering Geology 268:105525
607 doi:<https://doi.org/10.1016/j.enggeo.2020.105525>

608 Wilkinson P, Chambers J, Uhlemann S, Meldrum P, Smith A, Dixon N, Loke MH (2016) Reconstruction of
609 landslide movements by inversion of 4-D electrical resistivity tomography monitoring data Geophysical
610 Research Letters 43:1166-1174 doi:10.1002/2015gl067494

611 Wilkinson PB, Chambers JE, Meldrum PI, Gunn DA, Ogilvy RD, Kuras O (2010) Predicting the movements of
612 permanently installed electrodes on an active landslide using time-lapse geoelectrical resistivity data only
613 Geophysical Journal International 183:543-556 doi:10.1111/j.1365-246X.2010.04760.x

614 Zreda M, Shuttleworth WJ, Zeng X, Zweck C, Desilets D, Franz T, Rosolem R (2012) COSMOS: The cosmic-
615 ray soil moisture observing system Hydrology and Earth System Sciences 16:4079-4099

616

1
2
3
4
5
6
7
8
9
10
11
12
13
14
15
16
17
18
19
20
21
22
23
24
25
26
27
28
29
30
31
32
33
34
35
36
37
38
39
40
41
42
43
44
45
46
47
48
49
50
51
52
53
54
55
56
57
58
59
60
61
62
63
64
65

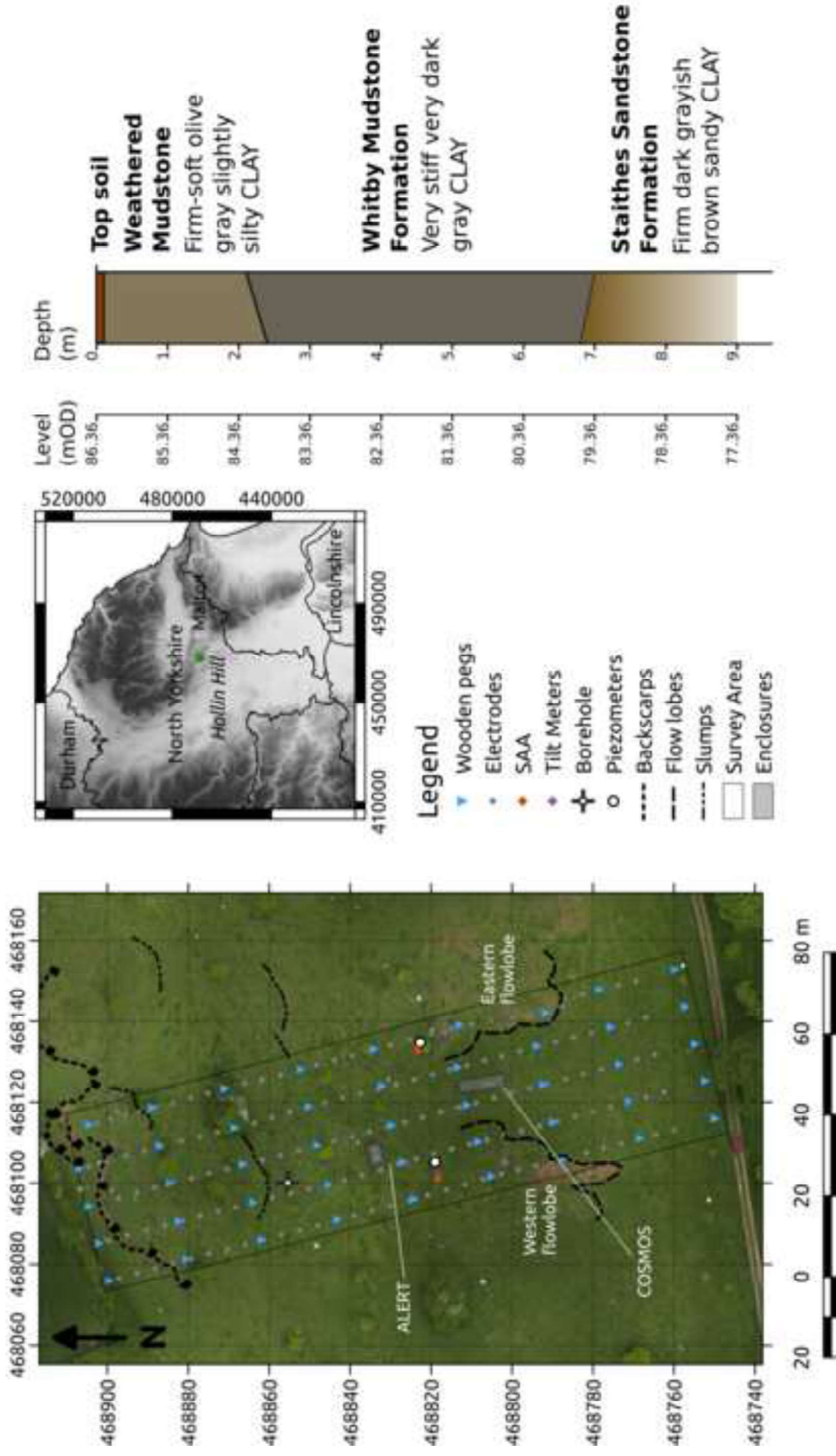
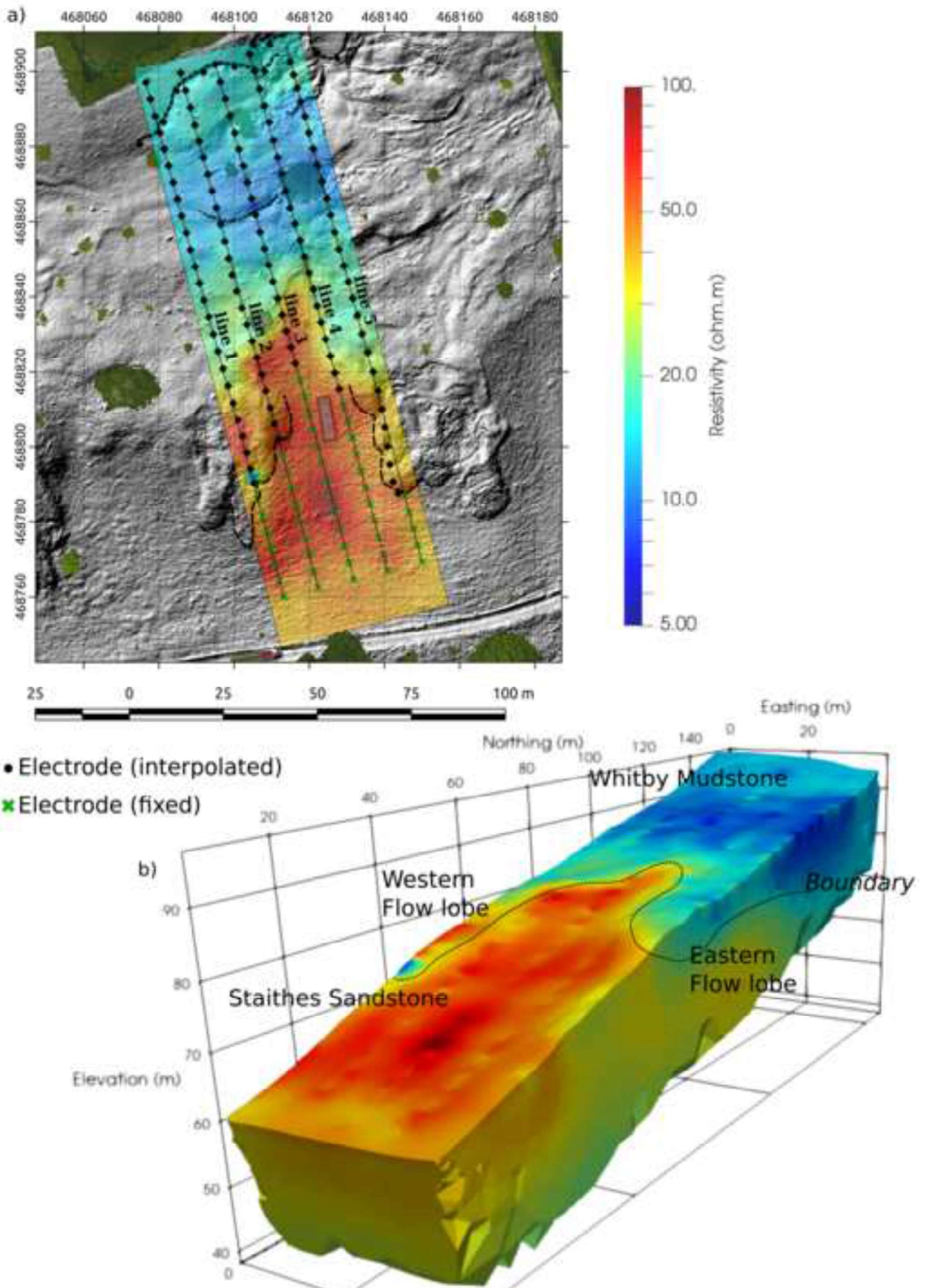
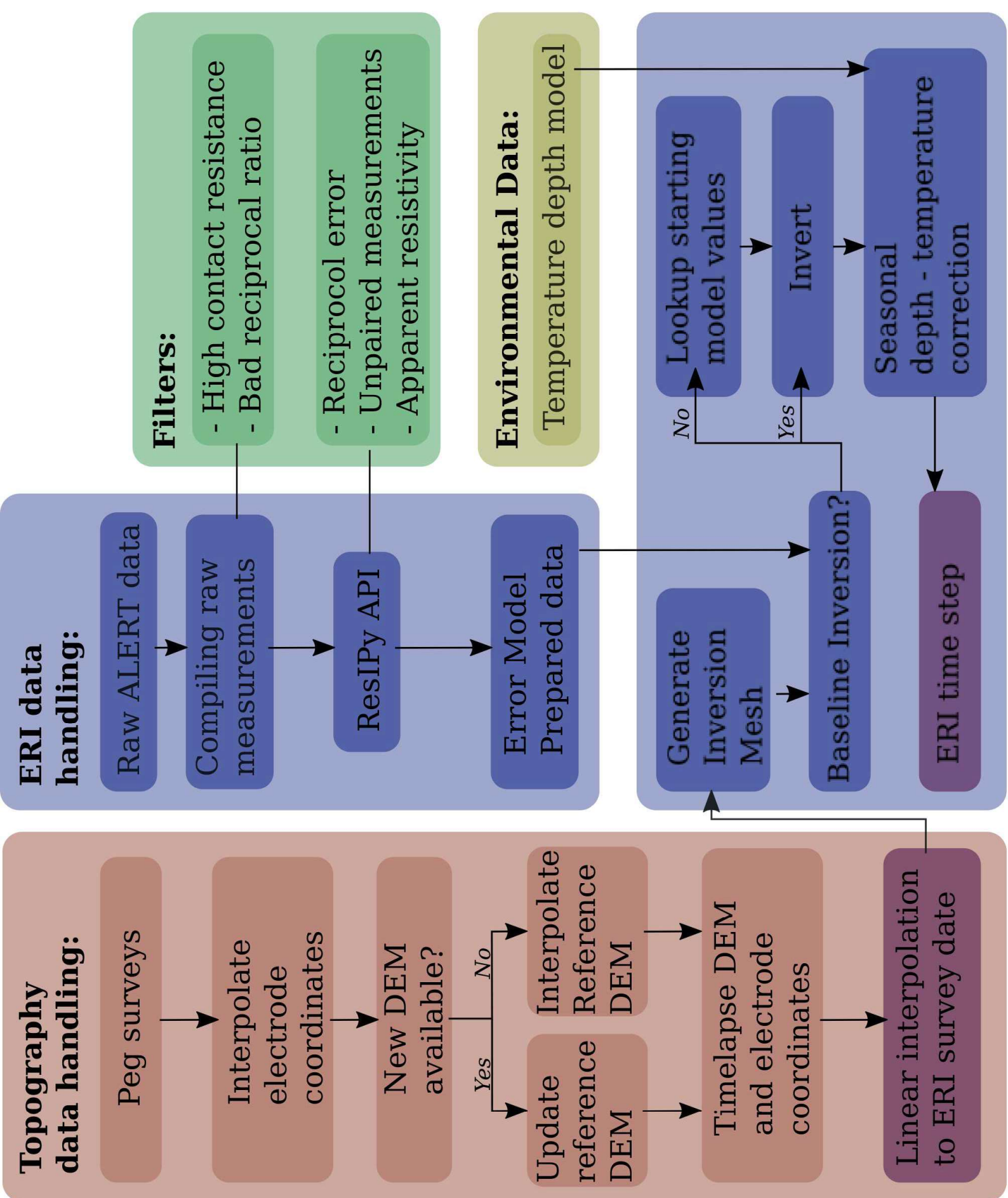


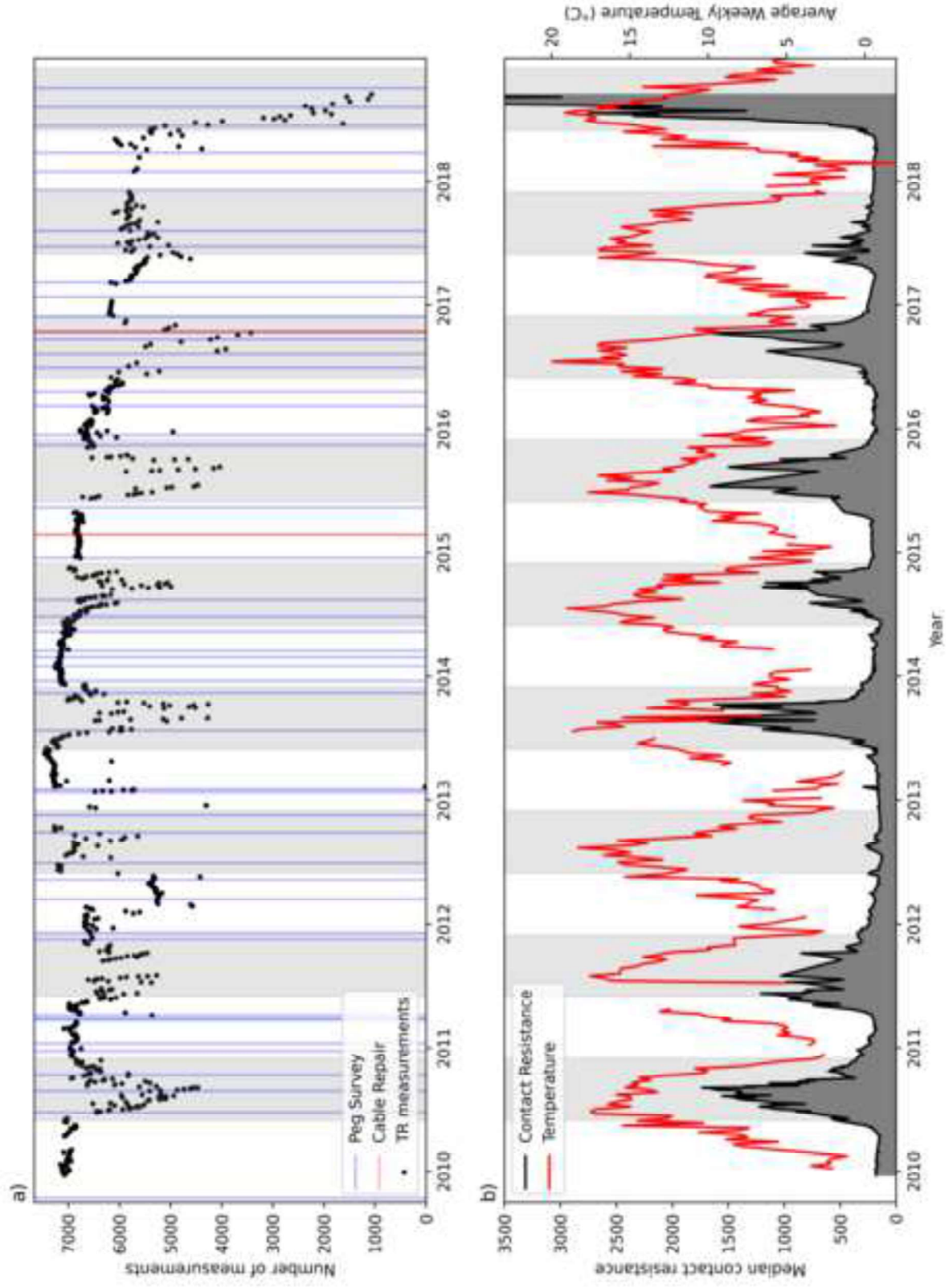
Figure 1

Figure 2

[Click here to access/download;Figure;Fig2.png](#)







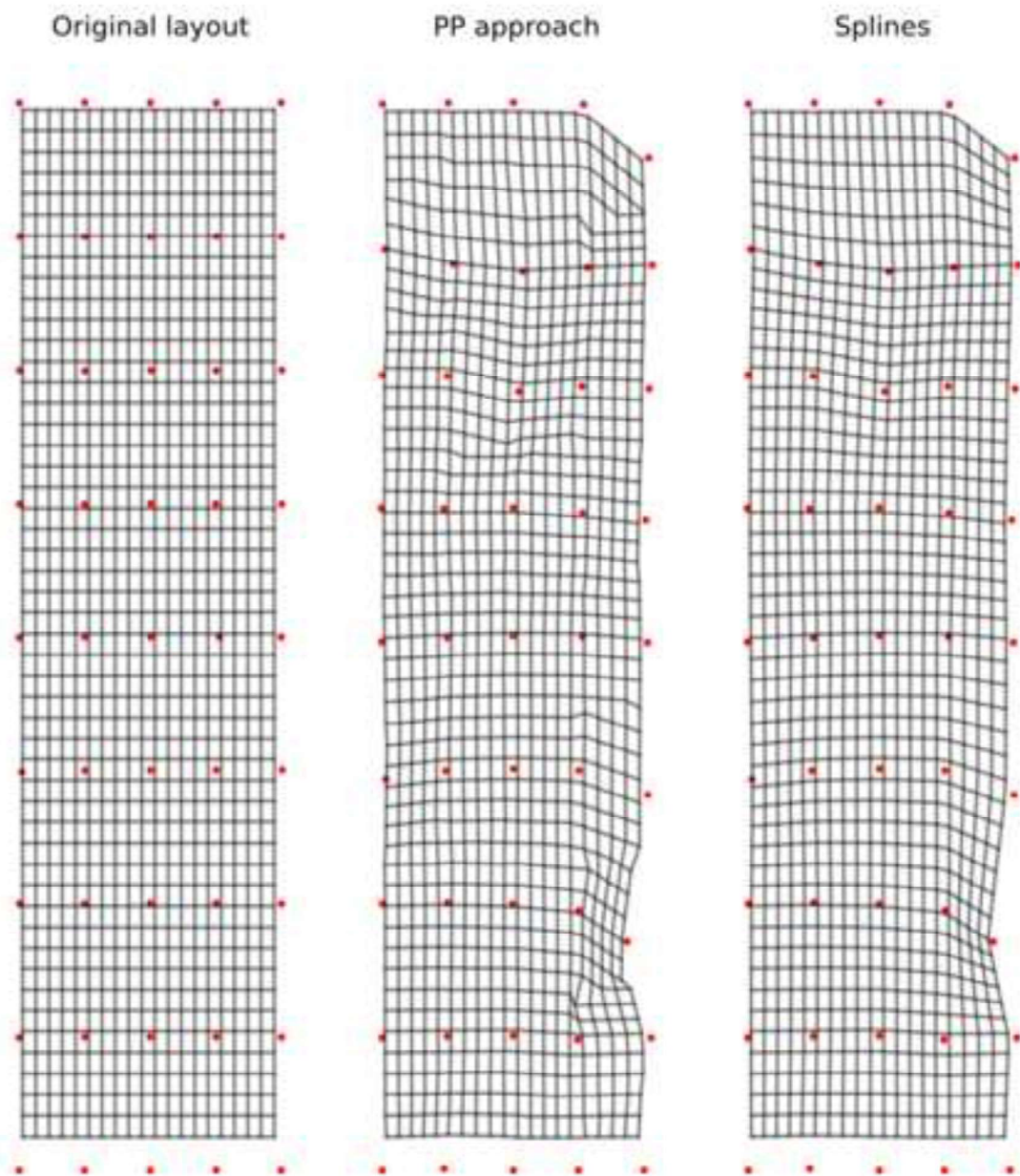
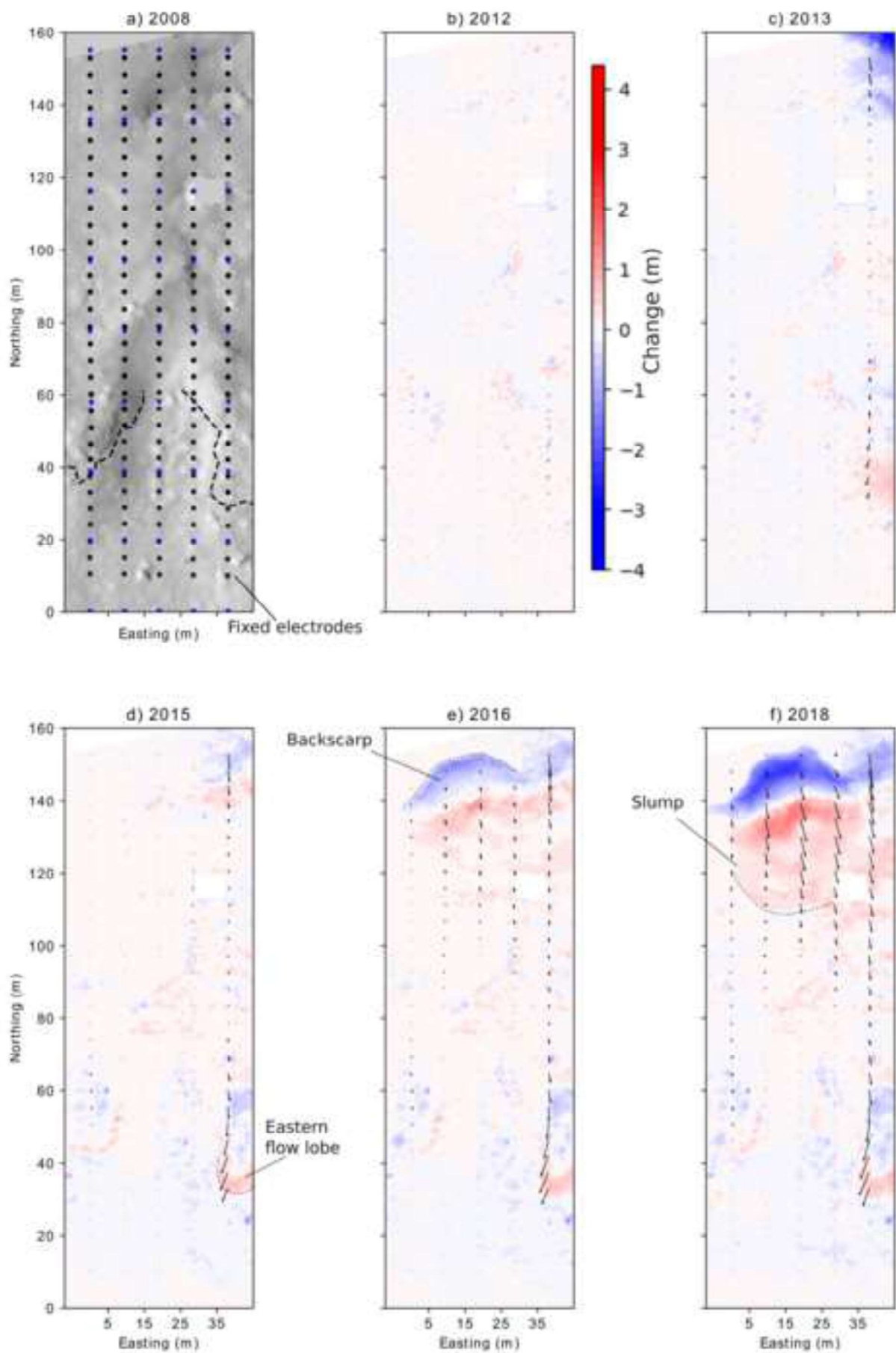


Figure 6

[Click here to access/download;Figure;Fig6.png](#)



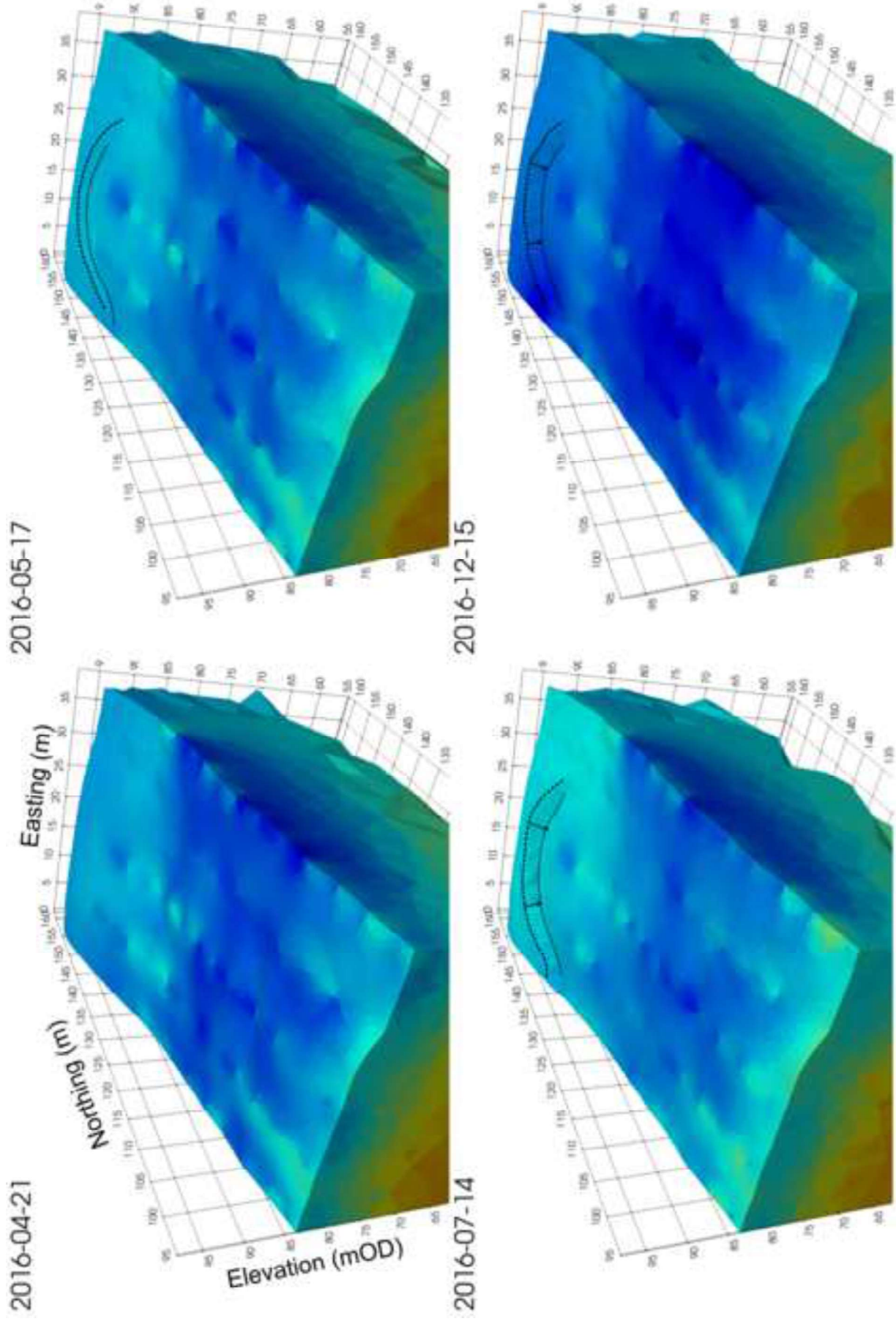


Figure 7

